

# Toward a Fundamental Understanding of Multiresolution SAR Signatures

Gilbert Leung and Jeffrey H. Shapiro

Massachusetts Institute of Technology  
Department of Electrical Engineering and Computer Science  
and Research Laboratory of Electronics  
Cambridge, Massachusetts 02139 USA

## ABSTRACT

A physical optics formalism is used to establish a first-principles analysis for discriminating specular returns from diffuse returns in a 1-D synthetic aperture radar. The optimum Neyman-Pearson detection processor is shown to substantially outperform the conventional, full-resolution SAR imager for extended specular targets embedded in diffuse clutter plus receiver noise. Significant performance advantages, relative to conventional full-resolution SAR processing, are also shown to accrue for optimum Neyman-Pearson reception of an extended diffuse target embedded solely in receiver noise.

**Keywords:** SAR signatures, multiresolution, detection, diffuse, specular

## 1. INTRODUCTION

Synthetic aperture radars (SARs) provide the coverage rate and all-weather operability needed for wide-area surveillance. SAR-based automatic target recognition (ATR) systems need fast and effective discriminators to suppress vast amounts of natural clutter from, while admitting the much more limited set of man-made object data to, their classification processors. Recent research, using mm-wave SAR data, has demonstrated that multiresolution processing offers a useful discriminant in this regard.<sup>1</sup> Other work, with ultra-wide-band foliage-penetrating SAR data, has shown that adaptive-resolution imaging can exploit the aspect-dependent reflectivity of man-made objects.<sup>2</sup> Neither these studies, nor other related work,<sup>4</sup> have taken a principled approach—one based on the physical characteristics of the reflecting surfaces and SAR operation—to multiresolution SAR image formation and optimal target detection. The present paper is a first step toward such a fundamental assessment.

Using the physical optics formalism established in Park and Shapiro,<sup>3</sup> we consider multiresolution SAR image formation for a 1-D SAR, i.e., a continuous-wave down-looking sensor. We find that the carrier-to-noise ratios (CNRs) for diffuse and specular reflectors have different multiresolution signatures. Thus, although a diffuse reflector and a specular reflector of the same size have identical normalized CNRs when their SAR returns are processed over the full dwell time, these reflectors show substantially different behavior when processed over shorter time intervals. In particular, the “broad-side flash” phenomenon exploited by Chaney et al.<sup>2</sup> is clearly present in our specular CNR analysis. This specular CNR behavior directly impacts the structure and performance of the Neyman-Pearson optimal detector for such a reflector: for extended specular targets the optimum detection processor substantially outperforms the conventional, full-resolution SAR imager. Optimum detection processing also offers a significant performance advantage, compared to conventional SAR imaging, for the case of an extended diffuse target.

## 2. 1-D SAR PRINCIPLES

The essential principles that permit multiresolution imaging to distinguish specular returns from diffuse returns can be gleaned from simple physical arguments, as we now show.

---

Send correspondence to J.H. Shapiro. Email: jhs@mit.edu; Phone: 617-253-4607; Fax: 617-258-7354.

Research supported by U.S. Air Force Office of Scientific Research Grant F49620-93-1-0604.

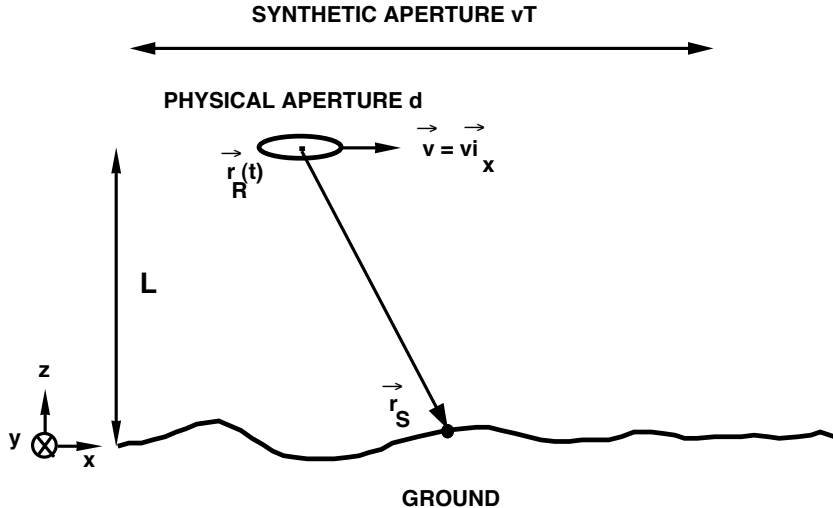


Figure 1. Geometry for a 1-D continuous-wave synthetic aperture radar.

## 2.1. Doppler Pulse-Compression Imaging

Consider the simple continuous-wave (cw) downlooking radar imager sketched in Fig. 1. A plane flying at speed  $v$  and height  $L$  above the ground collects returns, i.e., reflections, from the scatterers it irradiates. Because of the plane's motion, the Doppler-shift time history associated with the return from a point scatterer located at  $\vec{r}_s$  is a linear function—a frequency chirp—of rate  $\dot{\nu}_D = -2v^2/\lambda L$ , with zero-intercept at  $x/v$ , where  $x$  is the along-track component of  $\vec{r}_s$ , and  $\lambda$  is the radar's operating wavelength. The time duration of the chirp from this single scatterer is the dwell time, i.e., the length of time during which the particular scatterer lies within the radar's transmitter beam, given by  $T \approx \lambda L/vd$  in diffraction-limited far-field operation with an antenna of diameter  $d$ . By analogy with pulse compression operation of an angle-angle imager, we can show that matched-filter (chirp-compression) processing of the return from this single point scatterer will yield a time-domain output waveform that is centered at  $x/v$  and has a nominal width  $x_{res}/v$ , where

$$x_{res} \approx \frac{v}{|\dot{\nu}_D|T} \approx \frac{d}{2} \ll \frac{\lambda L}{d}, \quad (1)$$

gives the along-track spatial resolution of the system.

## 2.2. Diffuse versus Specular Reflections

The simple, point-scatterer description we have given for the resolution capability of a 1-D SAR applies directly to returns from an extended rough surface, i.e., to a diffuse reflector, but it does not apply directly to the returns from an extended smooth surface, i.e., a specular reflector. As sketched in Fig. 2, the returns from each point on a rough surface add incoherently, whereas the returns from each point on a smooth surface add coherently. In particular, the rough surface shown in Fig. 2 will produce a total return whose time duration equals the time this surface spends within the radar's transmitter beam. On the other hand, the smooth surface shown in Fig. 2 will produce a total return whose time duration is determined by the time it takes the radar's receiver antenna to move through the diffraction pattern created by the reflected wave. For a large specular target this time duration will be much less than the dwell time  $T$  given in the previous section. Furthermore, because of Snell's law, the tilt of such a specular target will lead to a time offset in the return field arriving at the radar receiver.

## 3. SYSTEM MODEL AND CNR

In order to quantify the phenomena described qualitatively in the preceding section, we shall extend the physical optics 1-D SAR analysis of Park and Shapiro<sup>3</sup> to include specular, as well as diffuse, reflectors, and multiresolution, as well as full-resolution imaging.



**Figure 2.** Left figure: rough surfaces give diffuse reflections. Right figure: smooth surfaces give specular reflections.

### 3.1. IF Signal Model

The intermediate-frequency (IF) signal in the SAR receiver can be taken to have complex envelope  $\mathbf{r}(t) = \mathbf{y}(t) + \mathbf{w}(t)$ , where  $\mathbf{y}(t)$  represents the return waveform and  $\mathbf{w}(t)$  is a zero-mean circulo-complex, white Gaussian receiver noise with spectral density  $N_0$ . In a convenient normalization, and assuming a multiplicative target model,<sup>3,5</sup> the return complex envelope can be written in the following form:

$$\mathbf{y}(t) = \sqrt{P_T} \int d\vec{\rho} T(\vec{\rho}) \xi_L^2(\vec{\rho} - \vec{v}t), \quad (2)$$

where  $P_T$  is the transmitter power,  $T(\vec{\rho})$  is the field-reflection coefficient vs. the transverse coordinate vector  $\vec{\rho} \equiv (x, y)$  on the  $z = 0$  reference plane, and  $\xi_L(\vec{\rho})$  is the normalized transmitter field pattern on this reference plane. In this equation, we have assumed that the radar's transmitter and receiver use the same antenna pattern, and that lag angle compensation has been performed. We shall assume that  $\xi_L$  results from  $L$ -m far-field free-space propagation of an elliptical Gaussian beam whose major and minor axes coincide with the across-track and along-track directions, respectively. The choice of a Gaussian pattern is for analytical convenience; the use of an elliptical pattern allows the across-track resolution to gain the superior resolution of a larger aperture dimension while the along-track resolution benefits from synthetic aperture processing.<sup>3</sup> Our model for a simple extended diffuse reflector is statistical:  $T(\vec{\rho})$  is a zero-mean, circulo-complex Gaussian random field with a  $\delta$ -function covariance,

$$\langle T(\vec{\rho}) T^*(\vec{\rho}') \rangle = \frac{\lambda^2 \rho_d}{\pi} \exp(-2|\vec{\rho}|^2/a^2) \delta(\vec{\rho} - \vec{\rho}'), \quad (3)$$

where  $\rho_d$  is the diffuse reflectivity and  $a$  is the radius of the reflecting region. Our corresponding model for a plane mirror of the same nominal size is essentially deterministic:

$$T(\vec{\rho}) = \sqrt{\mathcal{T}_s} \exp(-|\vec{\rho}|^2/a^2 + j2k\vec{\theta} \cdot \vec{\rho} + j\phi_s), \quad (4)$$

where  $\mathcal{T}_s$  is the intensity reflectivity,  $\vec{\theta} \equiv (\theta_x, \theta_y)$  is the tilt,  $\phi_s$  is the phase shift of the mirror, and  $k \equiv 2\pi/\lambda$  is the wave number at the radar wavelength. Because we seldom know the radar-to-ground distance to a small fraction of a wavelength, we shall assume that  $\phi_s$  is a random variable that is uniformly distributed on  $[0, 2\pi)$ ; the other parameters in our specular model are non-random. We have used Gaussian shapes in our diffuse and specular models because they will allow closed-form solutions for multiresolution CNR and other calculations while preserving the essential physical parameter dependencies of more realistic shape functions.

### 3.2. Multiresolution Carrier-to-Noise Ratio

The architecture of a simple 1-D SAR receiver is shown in Fig. 3. It consists of a chirp-compression filter—whose integration interval has zero time-offset and duration  $T_c$ —followed by a video detector. The carrier-to-noise ratio of this receiver,  $\text{CNR}(t; T_c)$ , is defined to be the mean target-return power in the cw-SAR image at time  $t$  divided by the mean receiver-noise power in the cw-SAR image at time  $t$ . We are interested in seeing whether or not the qualitative differences between the diffuse and specular reflectors, described earlier, are indeed present in the IF signal model we have posited. Specifically, does  $\text{CNR}(t; T_c)$  behave differently, for the diffuse and specular reflectors, as the processing time  $T_c$  is increased from very small values up to the full dwell time  $T$ ?

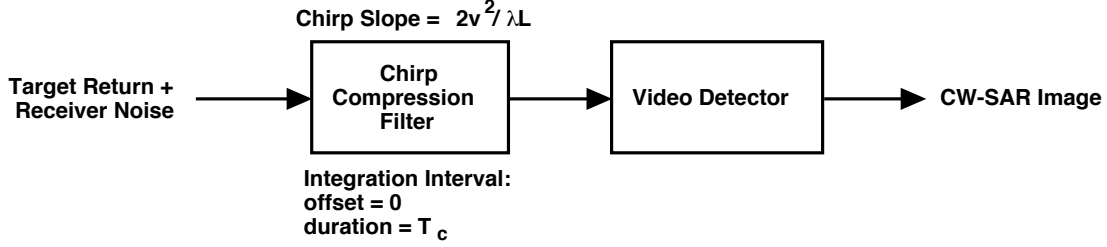


**Figure 3.** Block diagram of a 1-D SAR receiver.

Using the model given in the previous section, we find that the diffuse target's CNR obeys

$$\text{CNR}(t; T_c) = K_d \rho_d T_c \exp \left[ -\frac{(vt)^2}{\Delta x_d^2} \right], \quad (5)$$

and the specular target's CNR is given by,

$$\text{CNR}(t; T_c) = K_s \frac{k^2 a^2 T_s T_c}{2} \exp \left[ -\frac{(vt - x_s)^2}{\Delta x_s^2} \right], \quad (6)$$

where  $K_d$  and  $K_s$  are constants that do not depend on the processing time  $T_c$ . These equations show that the Doppler-compressed diffuse and specular returns have CNRs with different spatial extents  $\Delta x_d$  and  $\Delta x_s$ , respectively, and that the Doppler-compressed specular return has a spatial offset  $x_s$  that the corresponding diffuse case does not. These forms are indicative of the signatures we had hoped for: different resolutions ( $t$ -widths of  $\text{CNR}(t; T_c)$ ) for the specular and diffuse returns arising from the coherent nature of the specular reflection process, and an offset for the specular return that is due to Snell's law. Figure 4 shows that the desired signatures do, in fact, exist. In obtaining the curves in Fig. 4 we have assumed that: the radar's receiver is in the far field of the specular target; the radar's integration interval is long compared to the aperture-translation time and short compared to the target-dwell time; and the target is much larger than the along-track aperture size of the radar transmitter.

Figure 4 shows that the diffuse-target resolution follows a straight reciprocal dependence on the processing time. This is to be expected because  $T_c$  is large enough to form a significant synthetic aperture, but small enough that the full, dwell-time limited synthetic aperture is not used. The more interesting part of Fig. 4 is the specular target behavior. At short processing times the resolution is limited by the target's size, and independent of  $T_c$ . Ultimately,

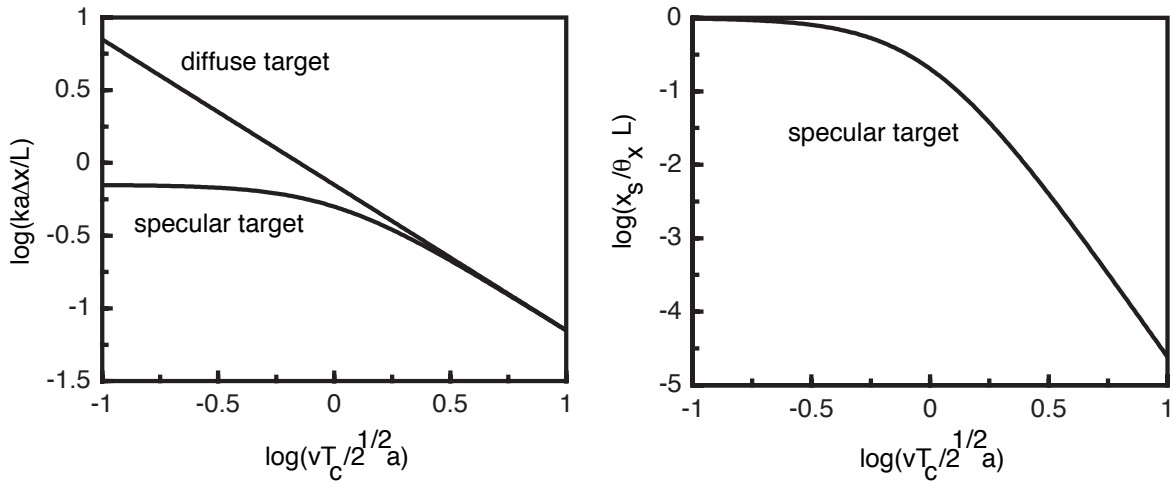


**Figure 4.** Left figure: specular vs. diffuse target resolution. Right figure: specular target angular shift.

the synthetic aperture effect takes over, and the specular curve merges with the diffuse curve. For our equal-sized specular and diffuse targets, this means their full-resolution (dwell-time limited processing) images will have the same  $\Delta x$  values. Figure 4 also shows the aspect dependence of the specular return. Here we see that geometric optics (Snell's law) behavior prevails at short processing times, but the tilt dependent shift in the SAR image disappears as the processing time is increased.

#### 4. TARGET DETECTION THEORY

Our final task will be to show that the multiresolution signatures demonstrated in the last section have important implications for target detection. To do so, we study the idealized problem of detecting an extended specular target embedded in diffuse clutter plus receiver noise. To further explore the realm of optimal detection processing, we go on to address the optimal detection of an extended diffuse target embedded in receiver noise alone.

##### 4.1. Specular Target in Clutter plus Noise

Consider the following idealized binary hypothesis testing problem. Under hypothesis  $H_0$ , the normalized IF complex envelope satisfies,

$$\mathbf{r}(t) = \mathbf{y}_d(t) + \mathbf{w}(t), \quad (7)$$

where  $\mathbf{y}_d(t)$  is the return from a statistically homogeneous diffuse clutter, i.e.,  $\mathbf{y}_d(t)$  is given by Eq. 2 for a diffuse reflector whose covariance function is found from Eq. 3 with  $a \rightarrow \infty$ . Under hypothesis  $H_1$ , we have that

$$\mathbf{r}(t) = \mathbf{y}_s(t) + \mathbf{y}_d(t) + \mathbf{w}(t), \quad (8)$$

where  $\mathbf{y}_s(t)$  satisfies Eq. 2 with  $T(\bar{\rho})$  from Eq. 4. Under either hypothesis,  $\mathbf{w}(t)$  is white Gaussian receiver noise.

The optimum Neyman-Pearson detection processor for this problem processes  $\mathbf{r}(t)$  to obtain maximum detection probability  $P_D \equiv \Pr(\text{say } H_1 \mid H_1 \text{ true})$  for a prescribed value of the false-alarm probability  $P_F \equiv \Pr(\text{say } H_1 \mid H_0 \text{ true})$ . Note that we will assume that this processor knows all the parameters of the diffuse and specular reflectors. (This same assumption will be made for the two suboptimum receivers described below.) In a real detection scenario, many of these parameters may be unknown and will have to be estimated from the data. Our desire here is to show that the multiresolution processor can offer significant performance improvement over a conventional, full-resolution SAR imager. If this is not the case in an idealized, known-parameter setting, it seems unlikely that any such advantage could prevail in more realistic situations.

The optimum detection problem we have posed is well known.<sup>6</sup> The structure of the optimum receiver is shown in Fig. 5; it consists of a whitening filter followed by a matched-filter/video-detector and then a threshold test. There are two other receivers whose performance we shall compare to that of the optimum system: the conventional, full-resolution 1-D SAR imager, and the optimized multiresolution 1-D SAR imager. These receivers share a common block diagram, shown in Fig. 6. The difference between these two receivers is as follows. The conventional imager uses no integration-interval offset in its chirp compressor. In other words, it makes no attempt to accommodate the Snell's law shift in the time at which the specular-target return occurs. Also, the conventional imager uses the full dwell time for its chirp compression integration; it does not try to exploit the multiresolution specular signature we demonstrated in the previous section. In contrast, the optimized multiresolution imager chooses its integration-interval offset and duration to maximize the resulting  $P_D$  at the prescribed  $P_F$ . This receiver represents an idealized, known-parameter 1-D SAR version of the aspect-dependent processor reported by Chaney et al.<sup>2</sup>

The receiver operating characteristics ( $P_D$  vs.  $P_F$  behaviors) of the preceding three receivers share a common form,<sup>6</sup>

$$P_D = Q(d, \sqrt{-2 \ln P_F}), \quad (9)$$



**Figure 5.** Optimum Neyman-Pearson receiver for a specular target embedded in diffuse clutter plus receiver noise.

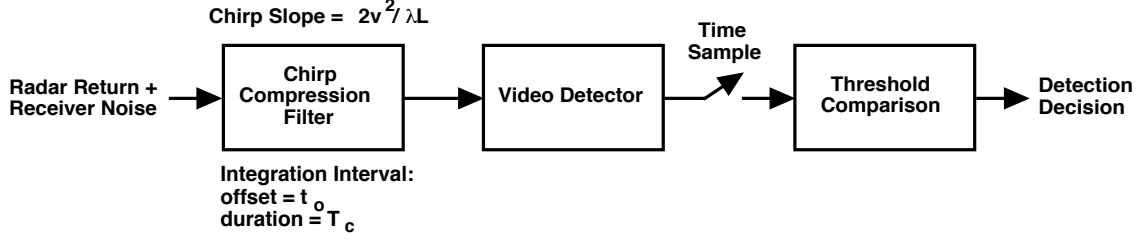


Figure 6. 1-D SAR imager receivers.

where

$$Q(\alpha, \beta) \equiv \int_{\beta}^{\infty} dz z \exp(-\alpha^2/2 - z^2/2) I_0(\alpha z), \quad (10)$$

is Marcum's  $Q$  function, and  $I_0$  is the zeroth-order modified Bessel function. In Eq. 9,  $d^2$  is the effective signal-to-noise ratio (SNR), which, in general, has a different value for each of our three receivers. We have plotted Eq. 9 for several  $d$  values in Fig. 7. The rest of our analysis shall concentrate on the behavior of the effective SNRs.

Let us use  $d_o^2$ ,  $d_c^2$ , and  $d_w^2$  to denote the effective SNRs for the optimum receiver, the conventional full-resolution 1-D SAR receiver, and the optimum white-noise receiver, respectively. The optimum white-noise receiver achieves maximum  $P_D$  at the allowed  $P_F$  for our binary hypothesis test when there is no diffuse clutter present under either hypothesis. It turns out that this receiver takes the form of an optimized multiresolution SAR imager in the absence of clutter, and is very nearly the optimized multiresolution SAR in the presence of clutter. The preceding effective SNRs are given by the following expressions:<sup>5</sup>

$$d_o^2 = \frac{\text{SNR}_o}{\text{DNR}_o} \sqrt{1 + \zeta^2} \mathcal{I}(\zeta, \xi, \text{DNR}_o), \quad (11)$$

$$d_c^2 = \frac{\text{SNR}_o}{\text{DNR}_o} \frac{2\zeta \sqrt{2(1 + \zeta^2)}/(1 + 2\zeta^2)}{1 + (\sqrt{2}/\text{DNR}_o)} \exp[-2\xi^2/(1 + 2\zeta^2)], \quad (12)$$

$$d_w^2 = \frac{\text{SNR}_o}{\text{DNR}_o} \frac{\exp[-\xi^2/(1 + \zeta^2)]}{[\sqrt{(1 + \zeta^2)}/(1 + 2\zeta^2)] \exp[-\xi^2/(1 + \zeta^2)(1 + 2\zeta^2)] + (1/\text{DNR}_o)}. \quad (13)$$

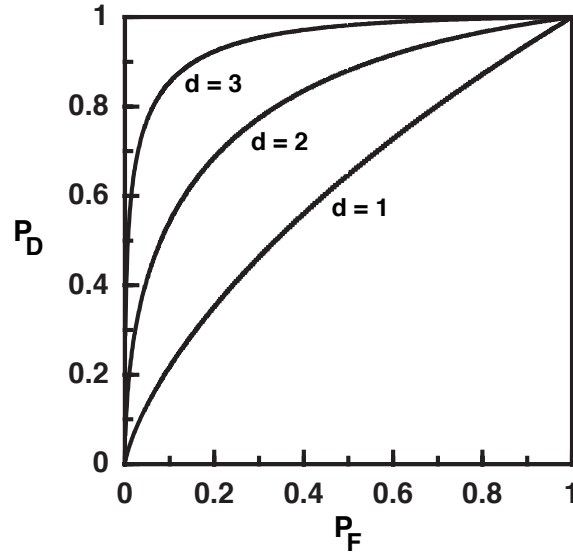


Figure 7. Marcum's  $Q$  function

In Eqs. 11–13,  $\text{SNR}_o$  is the peak signal-to-noise ratio for the specular target in the absence of along-track target tilt ( $\theta_x = 0$ ), given by,

$$\text{SNR}_o = \frac{\sqrt{\pi} P_T \mathcal{T}_s k^3 a_x^2 a_y^2 a^3}{\sqrt{8} N_0 L^3 v \sqrt{1 + \zeta^2}} \exp(-2k^2 \theta_y^2 a^2), \quad (14)$$

and  $\text{DNR}_o$  is the diffuse clutter-to-noise ratio, given by,

$$\text{DNR}_o = \frac{\sqrt{\pi} P_T \rho_d a_x^2 a_y}{N_0 L^2 v}. \quad (15)$$

These expressions in turn depend upon the radar and target parameters already specified in Sect. 3.1 plus:  $a_x$ ,  $a_y$ , which are the along-track and across-track beam waists of the radar's elliptically-Gaussian transmitter beam;  $\zeta \equiv a_x/\sqrt{2}a$ , which is the SAR's ultimate along-track resolution normalized by the target size;  $\xi \equiv k\theta_x a_x$ , which is the target's along-track tilt normalized by the radar's along-track diffraction-limited beam angle; and a normalized signal-to-noise-plus-clutter frequency integral,

$$\mathcal{I}(\zeta, \xi, \text{DNR}_o) \equiv \int df' \frac{\sqrt{\pi} \exp\{-(1 + \zeta^{-2})[\pi f' - \xi/(1 + \zeta^2)]^2\} \exp[-\xi^2/(1 + \zeta^2)]}{\zeta^2 \exp(-\pi^2 f'^2) + (1/\text{DNR}_o)}. \quad (16)$$

Note that  $\mathcal{I}(\zeta, \xi, \text{DNR}_o)$  satisfies,

$$\text{DNR}_o \frac{\exp[-\xi^2/(1 + \zeta^2)]}{(\text{DNR}_o + 1)\sqrt{1 + \zeta^2}} \leq \mathcal{I}(\zeta, \xi, \text{DNR}_o) \leq 1, \quad (17)$$

and has the following asymptotic behavior with respect to  $\text{DNR}_o$ ,

$$\lim_{\text{DNR}_o \rightarrow 0} \frac{\mathcal{I}(\zeta, \xi, \text{DNR}_o)}{\text{DNR}_o} = \frac{\exp[-\xi^2/(1 + \zeta^2)]}{\sqrt{1 + \zeta^2}}, \quad (18)$$

$$\lim_{\text{DNR}_o \rightarrow \infty} \mathcal{I}(\zeta, \xi, \text{DNR}_o) = 1. \quad (19)$$

Equation 17 implies that  $d_o^2 \geq d_w^2$  from Eqs. 11 and 13, as must be the case. Equation 18 guarantees that Eq. 13 reduces to Eq. 11 in the absence of clutter, as it should.

To demonstrate the advantage of optimal processing, we shall present calculated results for several interesting cases. We first consider the case in which along-track target tilt is not an issue, i.e.,  $\theta_x = 0$  in our specular target model. Figure 8 show log-log plots of the optimum receiver's effective SNR advantages ( $d_o/d_w$  and  $d_o/d_c$ ), as a function of normalized target size  $1/\zeta = \sqrt{2}a/a_x$ , for two values of the diffuse clutter-to-noise ratio  $\text{DNR}_o$ . We know that  $d_w \rightarrow d_o$  as  $\text{DNR}_o \rightarrow 0$ . Figure 8 shows that for extended specular targets, i.e., for  $\zeta < 1$  this equivalence prevails even when the clutter is strong. Physically, the large specular target presents a shorter-than-dwell-time return to the radar receiver. Hence, this return has a narrower bandwidth—less frequency chirp—than the clutter return. The performance of the white-noise receiver approximates that of the optimum receiver because the clutter spectrum is nearly flat over the bandwidth of the return from the extended specular, and hence the whitening filter in the optimum receiver is superfluous. Figure 8 shows that the optimum receiver has many decibels of effective SNR advantage over the conventional receiver for a large specular target ( $\zeta \ll 1$ ). The conventional receiver collects noise over the full chirp bandwidth of the dwell time, and this extra noise drives its SNR down, relative to that of the optimum receiver, because the optimum receiver uses the much narrower bandwidth associated with the more limited chirp present on the specular target return.

Our final specular-target calculation addresses the impact of target tilt. In Fig. 9 we have plotted  $d_o/d_c$  vs. normalized along-track tilt  $\xi$  at  $\zeta = 0.1$  for two values of  $\text{DNR}_o$ . Note that  $d_o \approx d_w$  prevails at this value of  $\zeta$ , so Fig. 9 also constitutes a comparison between conventional and optimized multiresolution SAR imagers. These curves underline the value of exploiting the aspect-dependence of the return from a large specular target.

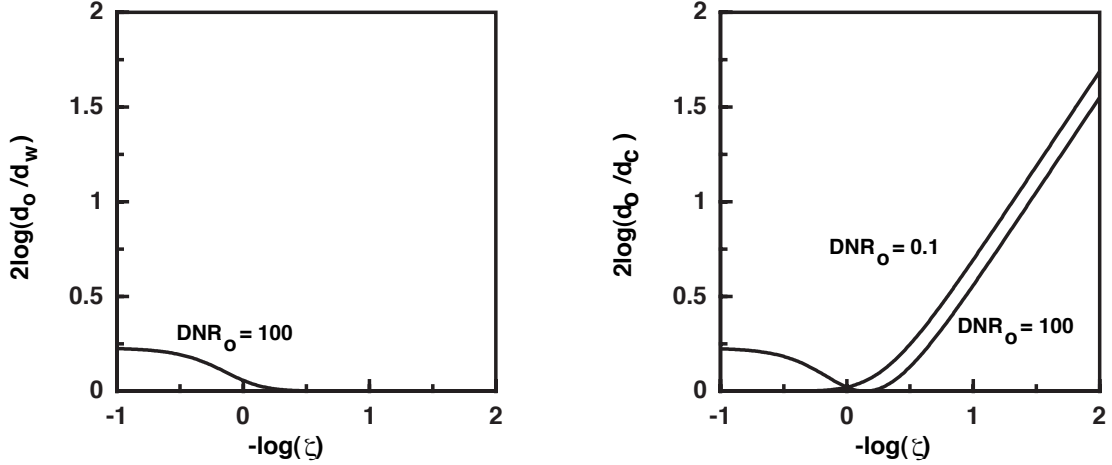


**Figure 8.** Effective SNR comparison. Left figure: optimum receiver vs. white-noise receiver at zero target tilt. The  $\text{DNR}_o = 0.1$  curve is indistinguishable from the  $d_o = d_w$  line. Right figure: optimum receiver vs. conventional receiver at zero target tilt.

#### 4.2. Diffuse Target in Receiver Noise

As another example of how optimal detection of extended SAR targets can differ from conventional, full-resolution SAR processing consider the problem of detecting an extended diffuse target embedded solely in receiver noise. Under hypothesis  $H_0$ , the normalized IF complex envelope now satisfies  $\mathbf{r}(t) = \mathbf{w}(t)$ , and under hypothesis  $H_1$  it now obeys  $\mathbf{r}(t) = \mathbf{y}_d(t) + \mathbf{w}(t)$ , where  $\mathbf{w}(t)$  is white Gaussian receiver noise, as before, but now  $\mathbf{y}_d(t)$  is given by Eqs. 2, 3 for a diffuse reflector of finite size  $a$ .

The optimum Neyman-Pearson receiver for the diffuse-target in white noise problem we have just posed follows readily from well known results on Gaussian signals in Gaussian noise.<sup>7</sup> One canonical form for the optimum receiver is the filter-squarer-integrator architecture shown in Fig. 10. The impulse response of the time-varying filter in this structure can be expressed as an infinite series involving the eigenfunctions and eigenvalues of the Karhunen-Loève (KL) expansion for  $\mathbf{y}_d(t)$ . For our Gaussian-antenna-beam/Gaussian-target-shape case, the necessary KL expansion turns out to be a standard Hermite-Gaussian series.<sup>5</sup> The eigenvalues from this series then permit straightforward calculation of the receiver operating characteristic for this receiver, with results as shown in Fig. 11. Here we have

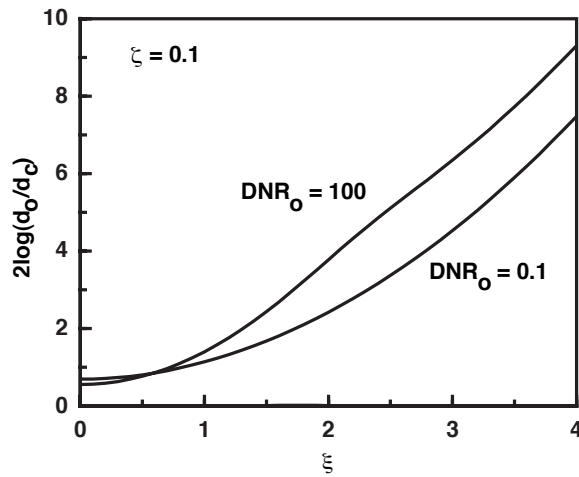


**Figure 9.** Effective SNR comparison: optimum receiver vs. conventional receiver as a function of along-track target tilt.

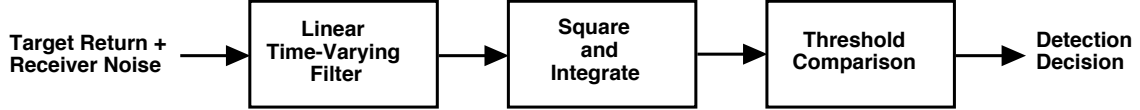


Figure 10. Optimum diffuse-target receiver: filter-squarer-integrator form.

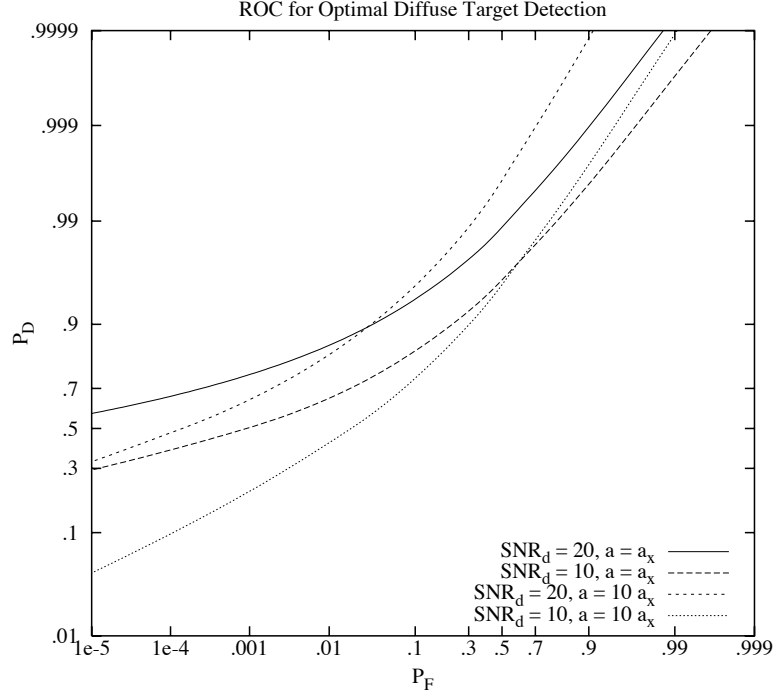


Figure 11. Performance of the optimum diffuse-target receiver

plotted  $P_D$  vs.  $P_F$  for two values of the diffuse-target signal-to-noise ratio,

$$\text{SNR}_d = \frac{\sqrt{\pi} P_T \rho_d k a_x a_y^2 a^2}{2 N_0 L^3 v}, \quad (20)$$

and two values of normalized target size  $a/a_x = 1/\sqrt{2}\zeta$ . For a fixed  $\text{SNR}_d$ , we see that the  $P_D/P_F$  curves for the two  $a/a_x$  values cross each other. This is characteristic of the Gaussian-signal in Gaussian-noise detection problem. At constant total SNR, there is an optimum diversity value which maximizes  $P_D$  for a particular  $P_F$ . In our case this translates into an optimum  $a/a_x$  value.<sup>5</sup>

The 1-D SAR imagers from Fig. 6—both the conventional full-resolution imager and the optimized multiresolution imager—can be applied to the diffuse-target detection problem. For the diffuse target case, the optimized multiresolution SAR imager no longer needs an integration offset, and its integration duration turns out to match the fundamental (maximum-eigenvalue) eigenfunction of the KL expansion for  $\mathbf{y}_d(t)$ .<sup>5</sup> The conventional SAR imager and the optimized multiresolution SAR imager have sufficient statistics which are exponentially distributed under both hypotheses. Consequently, we obtain the following simple results for their receiver operating characteristics:

$$P_D = \begin{cases} P_F^{1/[1+\text{SNR}_d\sqrt{2/(2+\zeta^{-2})}]}, & \text{for the conventional SAR receiver} \\ P_F^{1/\{1+2\text{SNR}_d/[1+\sqrt{(1+\zeta^{-2})}]\}}, & \text{for the optimized multiresolution SAR receiver} \end{cases} \quad (21)$$

Figure 12 compares the diffuse-target performance of the optimum Neyman-Pearson receiver, the conventional SAR imager and the optimized multiresolution SAR imager for two values of  $\zeta = a_x/\sqrt{2}a$  at  $\text{SNR}_d = 10$ . This figure

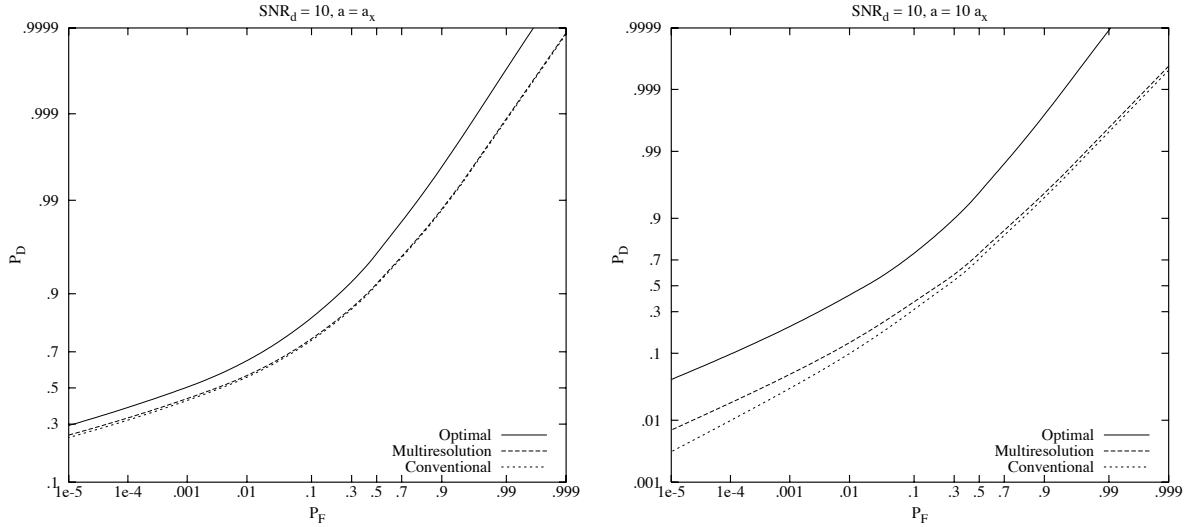


Figure 12. Diffuse-target performance comparisons

shows the expected behavior for the two SAR imagers, viz., the optimized multiresolution SAR imager begins to outperform the conventional SAR imager as the target size begins to exceed the ultimate along-track resolution capability of the radar. For this diffuse-target example, however, the optimized multiresolution SAR imager does not provide a close approximation to the optimum Neyman-Pearson receiver.

## 5. CONCLUSIONS

Our continuing objective is to develop a principled approach to the use of multiresolution image formation for discriminating specular returns from diffuse returns in synthetic aperture radar data. In this our initial effort, we have used a simple cw 1-D SAR model to establish the fundamental validity of using multiresolution, aspect-dependent specular target effects for the discrimination task. Complete derivations of our results are given in Leung,<sup>5</sup> where the more general specular-reflector case of an elliptically-symmetric curved mirror is considered. This source also includes target models and CNR behaviors for dihedral and trihedral reflectors. Our current work includes the extension of our formalism to 2-D stripmap operation, to polarimetric SAR, and to the detection and recognition of multicomponent targets.

## REFERENCES

1. W.W. Irving, A.S. Willsky and L.M. Novak, "A Multiresolution Approach to Discriminating Targets from Clutter in SAR Imagery," Proc. SPIE **2487**, 272-299 (1995).
2. R.D. Chaney, A.S. Willsky, and L.M. Novak, "Coherent Aspect-Dependent SAR Image Formation," Proc. SPIE **2230**, 256-274 (1994).
3. D. Park and J.H. Shapiro, "Performance Analysis of Optical Synthetic Aperture Radars," Proc. SPIE **999**, 100-116 (1988).
4. N.S. Subotic, B.J. Thelen, J.D. Gorman, and M.F. Reiley, "Multiresolution Detection of Coherent Radar Targets," IEEE Trans. Image Process. **6**, 21-35 (1997).
5. G. Leung, "Synthetic Aperture Radar Discrimination of Diffuse and Specular Target Returns," M.Eng. thesis, Dept. of Elect. Eng. and Comput. Sci., MIT, Feb. 1997.
6. H.L. Van Trees, *Detection, Estimation, and Modulation Theory: Part I*, Wiley, New York, 1968, Chap. 4.
7. H.L. Van Trees, *Detection, Estimation, and Modulation Theory: Part III*, Wiley, New York, 1971, Chap. 2.